Master's Thesis

Meso/micro-porous graphitic carbon for highly efficient capacitive deionization

Jihun Kang

School of Energy and Chemical Engineering
(Chemical Engineering)

Graduate School of UNIST

2018

Meso/micro-porous graphitic carbon for highly efficient capacitive deionization

Jihun Kang

Department of Chemical Engineering

Graduate School of UNIST

Meso/micro-porous graphitic carbon for highly efficient capacitive deionization

A thesis/dissertation
submitted to the Graduate School of UNIST
in partial fulfillment of the
requirements for the degree of
Master of Science

Jihun Kang

06. 26. 2018 of submission
Approved by

_____

Advisor
Ji-Hyun Jang

Meso/micro-porous graphitic carbon for highly efficient capacitive deionization

Jihun Kang

This certifies that the thesis/dissertation of Jihun Kang is approved.

06. 26. 2018 of submission

signature

_____

Advisor: Ji-Hyun Jang

signature

_____

Hyun-Kon Song

signature

_____

Jongnam Park

Abstract

Due to the scarcity of drinking water by population growth, global warming and increase in water consumption, the capacitive deionization (CDI) technology has considerable attention as a promising technology for desalination. Fast desalination rate and high electrosorption capacity are important element for desalination performance in CDI field. Here, meso/micro porous graphitic carbon spheres (mm-PGS) were fabricated using poly(vinyl alcohol), nickel chloride and fumed silica. Fabrication strategy of mm-PGS realized gram-scle production (>1.0 g mm-PGS sample per one time), high surface area (1492.8 $m^2 g^{-1}$) and large pore volume (5.1198 $cm^3 g^{-1}$). Under 100 ppm NaCl solution, the mm-PGS CDI electrodes showed rapid electrosorption rate (2.79 $g^{-1} min^{-1}$) and remarkable electrosorption capacity (9.37 mg g^{-1}) until 10 minutes compared with activated carbon electrodes (1.01 mg $g^{-1} min^{-1}$ and 8.07 mg g^{-1} for 23 minutes). The mm-PGS materials also exhibited a high rate constant (0.07146) through pseudo-second-order model as kinetic model, indicating that macro and mesoporous structure of mm-PGS is favorable for ion transport during desalination process. Furthermore, mm-PGS CDI electrode consumed low electrical energy per removed ions (33.17 kJ mol^{-1})

Contents

List of Figures

List of Tables

Chapter 1. Literature review

1.1 Water shortage

The shortage of drinking water due to environmental pollution and population growth will cause an important matter in near future. If the world population increases in the current pace and the water consumption per person continues to increase, one-third of world population will suffer a serious water shortage. World water resources are consisted of salt water (97.5 %) and fresh water (2.5 %). Salt water is existed in sea and some lakes, while fresh water is stored as underground water (30%) and snow/ice covering mountainous areas, Antarctic and Arctic (70 %), while only 0.3 % of fresh water is accessible by humankind. [1] Due to limited quantity of available fresh water, various desalination technologies to purify water from brackish water or sea have been strongly required accordingly.

1.2 Desalination

Desalination is a separation technology which is used to remove the dissolved salt of saline water. Desalination technology is essentially divided into two parts. One is treatment for water which has a low content of salt, and the other is treatment of the concentrated brine water which has much high salt concentration.

1.2.1 Worldwide used desalination technologies

Desalination of seawater and brine has attracted considerable attention to supply of fresh water for many countries in the world. Technological advancement in Reverse Osmosis (RO) desalination, Multi-Stage Flash (MSF) and Multi-Effect Distillation (MED) desalination during past decades shows great improvement in cost reduction, increase in flux and selectivity with reduced fouling. Thus, the RO, MSF and MED technologies have been utilized as widely used large scale desalination process around world. Fig. 1.2 exhibits global desalination technologies by capacity, indicating that RO, MSF and MED occupy 64 %, 23 % and 8 %, respectively. Global desalination with low occupied capacity is Electrodialysis (ED, 4%), while Fig. 1.2 doesn't show CDI technology because it hasn't been utilized as scale of industry yet, indicating that the CDI field needs significant improvement to compete other desalination technologies such as the well-established RO, MED and MSF. [2]

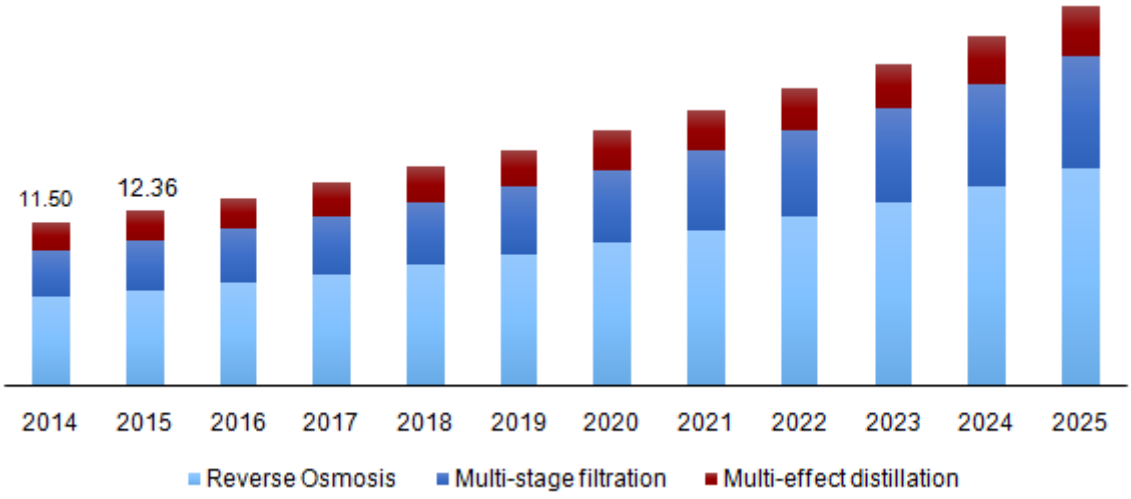

Figure 1.1. The Profit of three desalination technologies in the world market from 2014 to 2024. (USD Billion) [3]

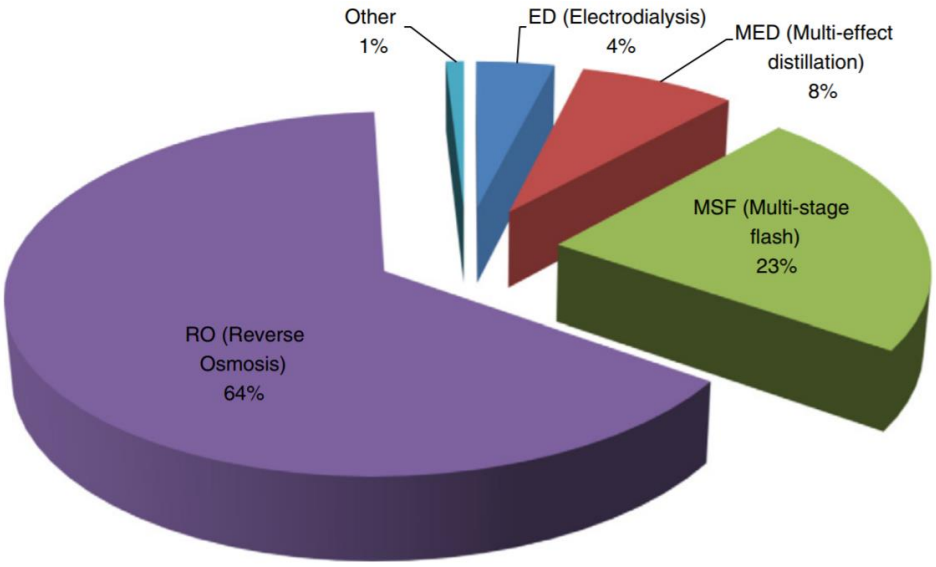

Figure 1.2. Global desalination technologies share by capacity. [2]

1.3 Capacitive deionization (CDI)

Among various water desalination technologies, the CDI has received considerable attention for various reasons: The CDI needs much small intrinsic energy (≈ 0.1-2.03 kWh m^{-3}) compared with RO technologies (≈ 3-8 kWh m^{-3}) which are widely utilized in desalination industry. Also, the processes of CDI including low-external potential (0.8-1.2 V) and low-pressure conditions and non-membrane design allow for low cost. In specific, the CDI is an environmentally friendly technology that does not make secondary pollution during desalination process.

1.3.1 Historical background

Following the concept of electrical double layer, broad studies on this field and other topics were started by Soffer, Oren and co-workers in the 1970s. This study still continues up to the present time. In reference, the work concentrated in advancement of new technology to prove effect of electrical double layer in porous carbon electrode and concluded that desalinating ions can be proceeded by small pores (0.5-3 nm). In 1978, Oren and Soffer show that idea of ‘‘four-action electrochemical parametric pumping cycles’’ was applied into efficient strategy to acquire division between deslinated water and concentrate. [4]

From the 1990s, many researchers concentrated in advancement of porous carbon material to desalinate water. Among many studies, Farmer et al. reported carbon aerogel materials to desalinate water and which drew keen attention. Fabricated carbon aerogel electrode exhibited considerable improvement of CDI performance compared with activated carbon as former CDI systems because monolithic structure, good conductivity and large internal surface area of carbon aerogel affects CDI results. [4]

Further study exhibits that ordered mesoporous carbon, carbide-derived carbon, carbon nanotube and graphene have been treated as active material of CDI electrede.

1.3.2 Principle of CDI: Electrical double layer (EDL)

The electrical double layer (EDL) can be defined as the region between two different phases that are formed at interface between electrolyte and micropores of porous carbon electrodes, anions and cation

are stored in positive electrode (anode) and negative electrode (cathode), respectively (Zhao, 2013). In 1883 (Elimelech, 1995), Helmholtz proposed the first model of EDL which explains the division of charges on EDL: charge accumulation on surface, while charges of opposite sign are accumulated at the electrolyte side as shown in Fig. 1.3(a). [5] In 1913, Gouy-Chapman developed a second model of EDL which considered the slope of charge density on interface, indicating that Thomas-Fermi screening distance and charge density changed by distance from surface of electrode are considered for second model. Also, this model included Boltzmann distribution as other factors owing to thermal effects (ions are not static), while described ions as point charges. Consequentially, second model predicted unrealistic high capacitance which is derived by very short distances from surface electrode. [6, 7] In 1924, Stern proposed new EDL model which assumes that ion distribution in "inner" region is followed by Langmuir's adsorption isotherm, while the region where long distance from surface of electrode is explained by the Gouy-Chapman model. [8]

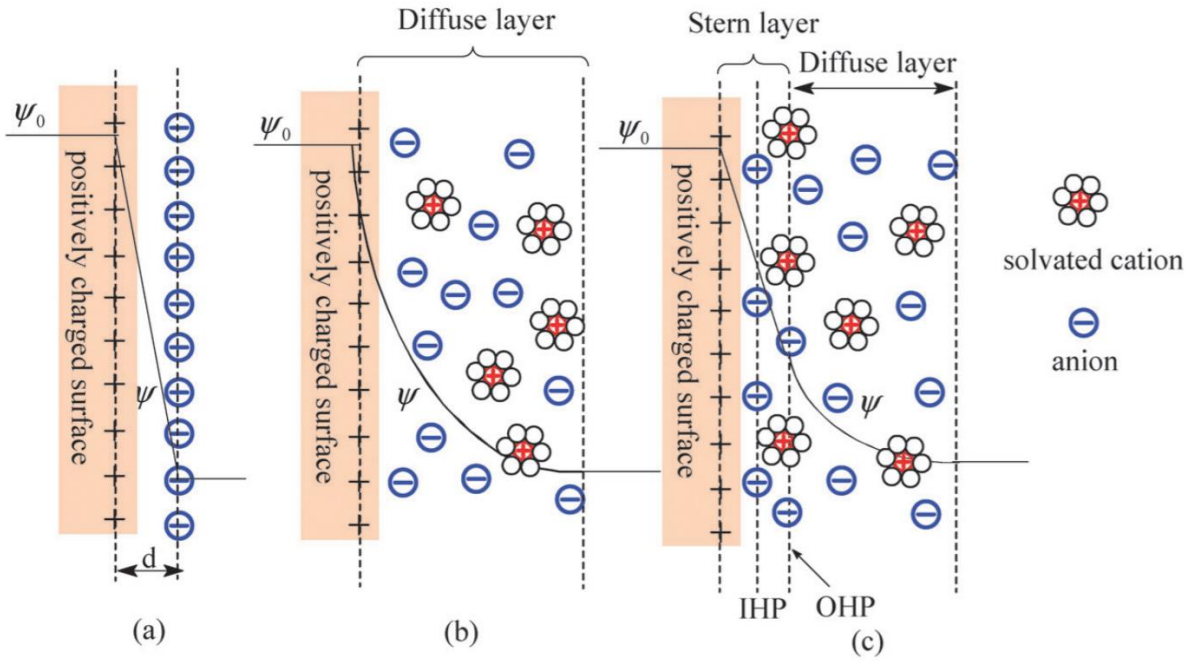

Figure 1.3. Scheme illustration of the electrical double layer (EDL) at interface between positive charged electrode and electrolyte: (a) the Helmholtz model, (b) the Gouy-Chapman model and (c) the Stern model. In Stern model, the Stern layer is composed of the inner Helmholtz plane and the outer Helmholtz plane. In Helmholtz model, d is the distance of double layer. ψ_0 and ψ are indicated as the potential at charged surface of electrode and interface between electrode and electrolyte, respectively. [9]

1.3.3 Process and performance of CDI

The CDI cell is composed of paralleled two porous carbon electrodes which can adsorb ions under applying external potential, as shown in Fig. 1.4. The ions (positive and negative ions) are electro-adsorbed into EDL from the flow of water through a spacer which is positioned between the two paralleled electrodes. The CDI is based on forming the EDL inside the pores of carbon materials.

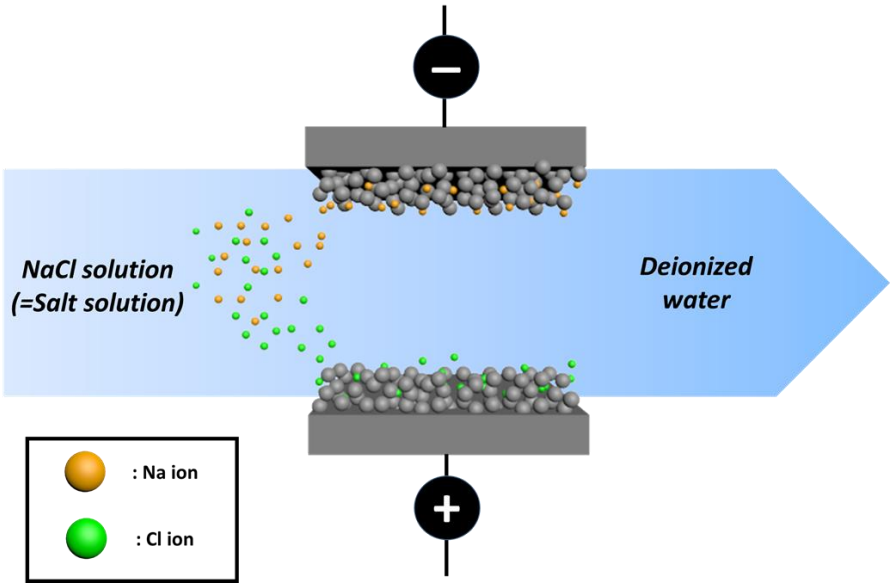

Figure 1.4. Schematic illustration of the CDI cell with water flow. When external potential applies to two paralleled electrodes, ions (Na^+ and Cl^-) moves to opposite charged electrode and are adsorbed into electrical double layer (EDL).

To check desalination performance by CDI technology, the variation of ion concentration over time is measured and interpreted. When desalination of various ions by CDI technology, collecting water sample and analyzing of ion composition have been done, while simple on-line measurement is enough to check single salt in solution with conductivity meter. Depending on position of conductivity meter, CDI method are divided into two types [4]:

The single-pass (SP) experiment uses storage tank and conductivity meter at exit position of the CDI cell or stack. The effluent concentration vs. time data is integrated to calculate total quantity of desalinated salt (the variation of feed water concentration and this variation is multiplied by the flow rate of water (Φ). [4]

The batch-mode (BM) experiment as another common approach requires much small recycling reservoir and conductivity is positioned in this container. In batch-mode experiment, the gap of salinity between the initial salt concentration and final salt concentration is multiplied by the volume of total salt water to calculate desalination performance. [4]

The capacitance of CDI materials are evaluated by cyclic voltammetry with 1.0 V of potential (typical operation value) is generally fixed in CDI experiment without faradaic contributions. The electro-adsorption behavior of active material is obtained from voltammogram and rectangular curve without faradaic (redox) reaction is good for electro-adsorption process. [10]

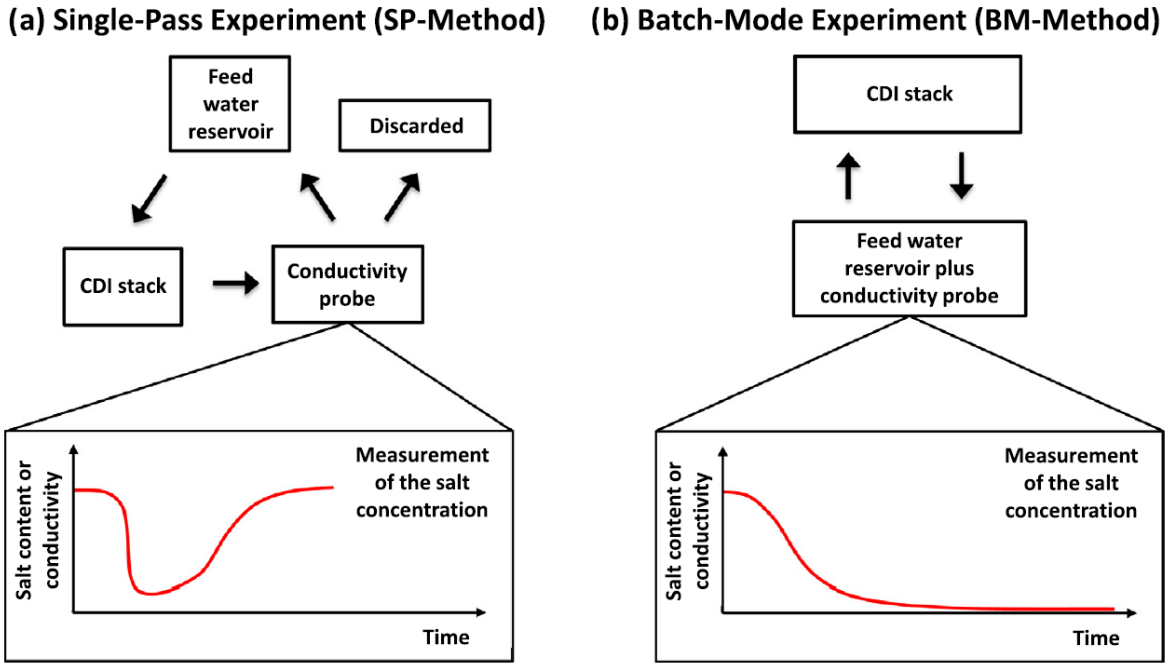

Figure 1.5. Schematic illustration of two CDI measurement methods: (a) Sing-Pass Experiment and (b) Batch-Mode Experiment. [4]

1.3.4 Feed-water composition

In CDI measurement, the feed water is divided by various type such as the analytical grade (particular amounts of ions in water) and the complex compositions (industrial water, domestic waste water, brackish water in natural and etc.). First, utilizing air-saturated water or not is important for measurement. When study use air-saturated water, the content of oxygen and carbon dioxide in water should be kept and reported. On the other hand, free water for oxygen and carbon dioxide condition requires nitrogen blanket or bubbling nitrogen gas in the water storage tank. Generally, feed water is divided by the following types:

① Real water (running water, underground water, diluted sea water and waste or process water from agriculture and industry) is composed of various ions (monovalent and divalent) and amphoteric ions (i.e., In accordance with pH in solution, electrical charge of ion changes, such as HCO_3^- and HPO_4^{2-}). Also, real water contains colloidal matter (such as humic acids).

② Imitated water by synthesized composite and simulating a ‘‘real’’ water source without solid particles, organic pollutants, and the like.

③ Single salt water (such as KCl and NaCl) is normally used in laboratory scale experiment

To calculate salt electro-adsorption capacity of CDI electrode, Number 3 condition is easy to analyze because the CDI results is strongly related with desalination time and conductivity meter in on-line. [4]

1.3.5 Electrode materials

The porous structure in carbon electrode is an important factor for CDI performance and this characteristic is similar with the capacitive energy storage devices. Until now, advancement and fabrication of porous structure in carbon electrode is main interest for both studies. Fig. 1.6 shows various carbon materials used for CDI application. Thus, morphology study (surface area, pore volume, pore size distribution and pore connectivity) are strongly related with CDI performance of carbon electrode. Furthermore, electronic conductivity and electrochemical stability are important to realize excellent CDI performance. The following list shows significant condition of carbon which is used as CDI electrode.

① Available surface area accessed by large ions

- Electrosorption capacity of salt is related to the surface area of carbon.
- Total surface area of carbon calculated from morphology study is not corresponded to valid area for ion access.

② Outstanding electro-chemical stability under used various pH conditions and potential window (no oxidation, etc.)

- Significant condition to ensure system stability and longevity.

③ The pore structure of carbon electrode which is favorable for ion mobility.

- Very small pores lead to disturbance for ion diffusion and kinetic limitation.
- The pore structure in carbon electrode (distances between particles and thickness of active material on current collector) is also considered.

④ High electrical conductivity

- In carbon materials, good electrical conductivity (such as metal and metal-like electrical conductivity) can create that total surface of active material is charged with small electrical potential.
- Only a low resistance guarantees a small energy consumption and small heating.

⑤ Small contact resistance at interface between the current collector and the active material

- To prevent potential drop from current collector to active material, a low contact resistance should be required.

⑥ Better wettability

- Hydrophilic property of electrode guarantees that total pore volume efficiently participates desalination process.

⑦ Expandability and low cost

- Considering cost is important element for expansion and industry field.

⑧ High processability

⑨ Large abundance in natural and low carbon dioxide foot printing

⑩ High bio stability

- Biofouling causes disturbance for long period operation of CDI in brackish water.

For fabrication of CDI electrodes, electrodes are prepared by method which is similar to energy storage device: carbon slurry are made by mixing of carbon material as active material, a conductor such as carbon black and a polymeric binder (usually ~10 wt %). The mixed carbon slurry is casted on graphite current collector which can prevent the corrosion in salt water and then coated electrode is dried to evaporate solvent. [4]

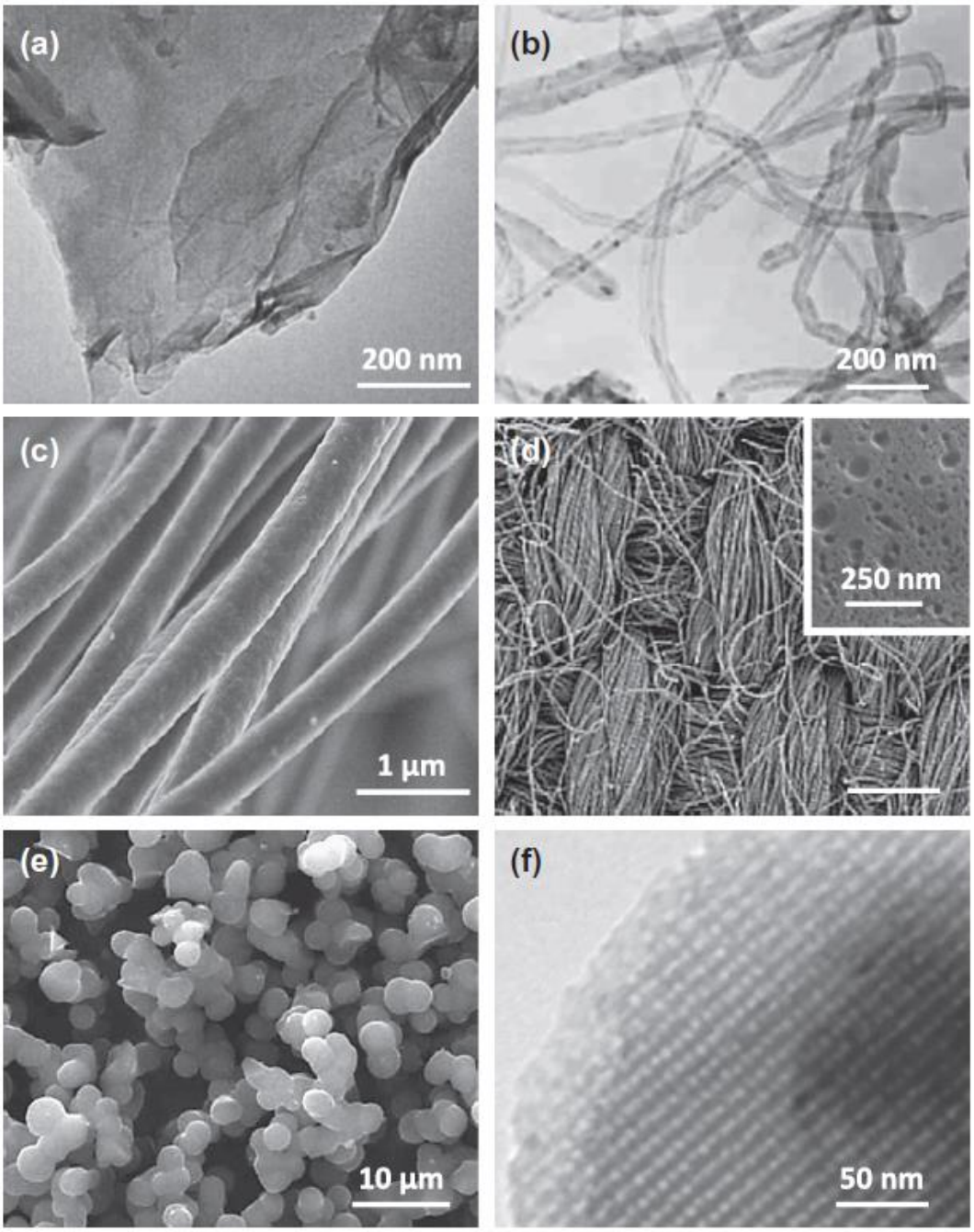

Figure 1.6. Utilized various carbon material in CDI application. (a) Graphene-like carbon flake [11], (b) multi-walled carbon nanotubes [12], (c) electro-spun fibers [13], (d) activated carbon cloth [14], (e) carbon aerogels [15], and (f) ordered mesoporous carbon [16].

1.4 Graphene

Graphene is one among various carbon allotropes such as carbon nanotube, fullerene and diamond. Graphene is composed of two-dimensional (2D) single sheet of carbon atoms. These carbon atoms are sequenced and formed a hexagonal structure. In 2004, the graphene was discovered by peeling off graphite with scotch tape. The ideal graphene sheets can be acquired by mechanical exfoliation technology and exhibits following characteristics: remarkable surface areas (2620 m^2 g^{-1}), highly ordered, outstanding Young's modulus (1 TPa), excellent thermal conductivity (5000 W mK^{-1}), excellent chemical stability and high electron conductivity (2.5 x 10^5 cm^2 V^{-1} s^{-1}) at room temperature. [17] Potential of graphene have been showed through various application such as transparent conducting electrodes (or composites), gas detection for single molecule, and energy storage devices (lithium ion battery and supercapacitor). Dimension of graphene is reduced

Furthermore, a distinct band gap of graphene can be achieved by decrease in dimension of graphene, indicating that graphene as semiconductive material can be used as application in transistors. There is no doubt that graphene has received considerable attention on the way of many study searching for new materials. [18]

1.4.1 Graphene electrode for CDI

Graphene can also be considered to CDI electrode due to outstanding characteristics. [19] In CDI field, graphene electrodes was treated by Wang et al and Li et al. After this study, new graphene electrode consisted of graphene flake, graphite powder and polymeric binder (72:20:8 weight ratio) is investigated. [4] Graphene foams as active material for CDI were fabricated by mixing of graphene oxide suspension and polystyrene microspheres (diameter: 280 nm) using ultrasonication. Graphene/polystyrene compound was separated through vacuum filtration and then sample is heated at 900 ^oC. Lastly, three-dimensional graphene which has hierarchical porous structure was prepared through combining an *in situ* defect etching method and template-directed strategy. [20] Graphene study for CDI are still underway to realize high electrosorption performance.

Chapter 2 Materials and methods

2.1 Fabrication of mm-PGS

Deionized water was mixed with Poly(vinyl alcohol) [M_w 31,000~50,000] (PVA) as carbon precursor to adjust weight ratio (10 wt %, PVA: Deionized water = 1: 9). PVA solution was heated at 80 ^oC for 4 hours. Then, Nickel chloride hexahydrate ($NiCl_2 \cdot 6H_2O$) as catalyst is introduced into PVA-deionized water solution and mixed for several times. Fumed silica (200-300 nm average particle size) as template was mixed in ethanol. Mixed silica solution was dried in conventional oven to obtain agglomerated silica sample and then dried silica particles are wetted by $NiCl_2 \cdot 6H_2O$-PVA-deionizaed water solution. Wetted silica sample was dried in conventional oven to remove water. Dried powder sample was putted into furnace and heated at 1000 ^oC for 30 minutes under hydrogen (H_2) gas and argon (Ar) gas. Carbonized sample was etched by hydrofluoric acid (HF) and hydrochloric acid (HCl) to remove silica template and nickel clusters. Etched carbonized sample was treated by second carbonization step under same condition to remove functional groups on surface of sample. Then, meso/micro porous graphitic carbon spheres (mm-PGS) were fabricated.

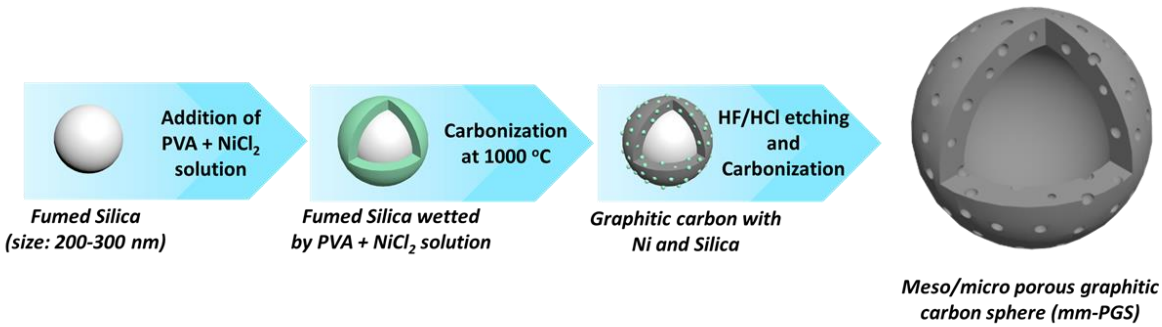

Figure 2.1. Schematic illustration of the mm-PGS fabrication.

2.2 Characterization of activated carbon (AC) and mm-PGS.

Surface morphology and structure of samples were measured by scanning electron microscope (SEM) and transmission electron microscopy (TEM) (JEM-2100, JEOL). Raman spectra of samples were characterized by WITec alpha300R with 532 laser as the light source for excitation. The N_2 adsorption desorption isotherm (BELSORP-max, BEL Japan Inc.) was conducted at 77 K. The pore size distributions of samples were acquired by Barrett-Joyner-Halenda (BJH) method for the N_2 adsorption desorption isotherm. X-ray photoelectron spectroscopy (XPS) (K-alpha XPS) was measured to check the chemical structure.

2.3 Electrochemical experiments

2.3.1 Preparation of electrode

The electrochemical electrodes were fabricated by carbon slurry which is composed of 80 wt % of active material, 10 wt % of polyvinylidene fluoride (PVDF) dissolved in N-Methyl-2-Pyrrolidone (NMP) and 10 wt % of acetylene black. The graphite sheets as current collector were coated by mixed carbon slurry and coated graphite sheets were dried at 150 ^{o}C for 10 hours.

2.3.2 Cyclic voltammetry

The electrochemical results of fabricated electrodes were analyzed by cyclic voltammetry (CV) in 1 M NaCl solution. The CV was measured by electrochemical instrument (VMP3 biologic) with 3-electrode system which is composed of fabricated electrodes as working electrode, Ag/AgCl (saturated by KCl) electrode as reference electrode and Pt mesh as counter electrode. The capacitance (C, F g^{-1}) was calculated by CV curve results using following Eq. (1):

$$C = \int i(V)dV / (2m\Delta Vv)$$

Where *i(V)* is current response, *m* is the mass of electrode (g), ΔV is the potential window and *v* is the potential scan rate.

2.3.3 Electrochemical impedance spectroscopy

Results of electrochemical impedance spectroscopy (EIS) were obtained at a frequency range from 100 kHz to 0.1 Hz using the same experiment condition (CV measurement).

2.4 Electrosorption experiments

2.4.1 Experiment condition and electrosorption capacity

The CDI electrode was fabricated with 8 cm x 8 cm graphite sheet as current collector by same method (Preparation of electrode in electrochemical experiments). Batch-mode CDI measurements were conducted and utilized to analyze the CDI performances of samples electrodes. All CDI measurement were conducted in various NaCl solution (100, 250 and 500 mg L^{-1}) with a 30 mL, the flow rate and the temperature of NaCl solution were kept at 30 mL min^{-1} and 298 K, respectively. CDI electrodes is applied by a constant potential (1.2 V) and conductivity meter which is positioned at an outside of CDI cell to measure conductivity change.

The electrosorption capacity (Γ, mg g^{-1}) was calculated by Eq. (2):

$$\Gamma = \frac{(C_0 - C_e) \cdot V}{m}$$

where C_0 is the initial NaCl concentration (mg L^{-1}), C_e is the final NaCl concentration (mg L^{-1}) at equilibrium for NaCl adsorption, V is the volume of the NaCl solution (L), m is total mass of active material on electrodes (g).

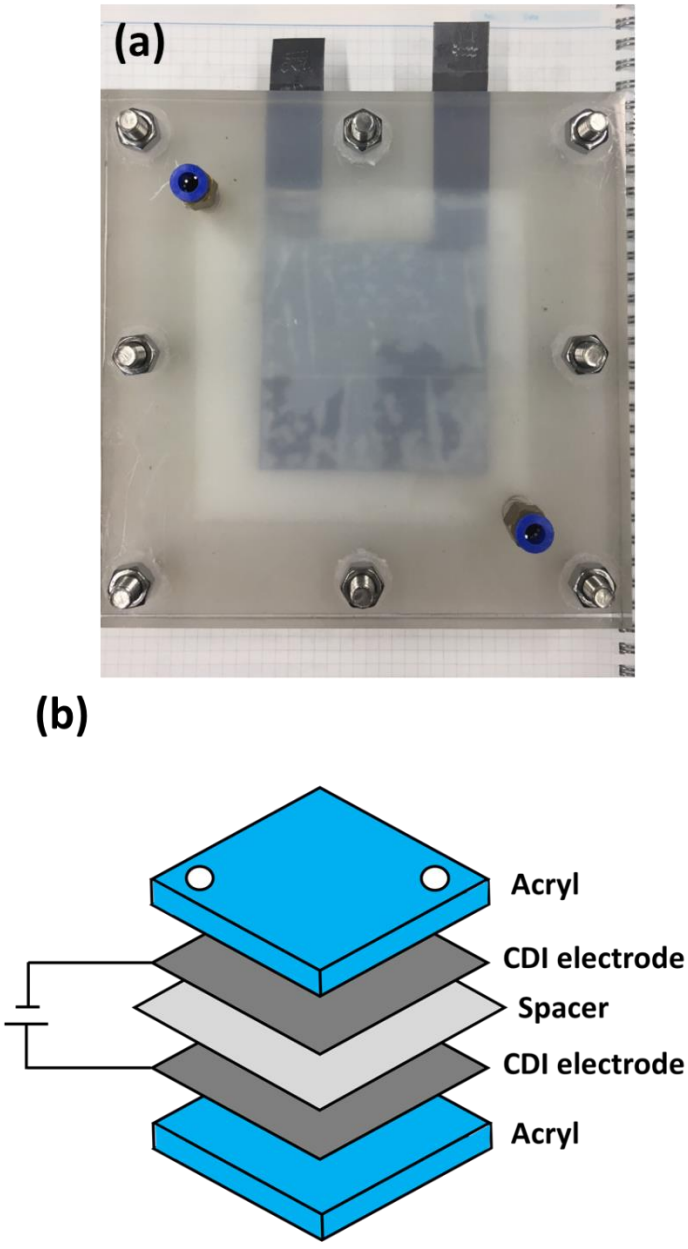

Figure 2.2. (a) Photographic image and (b) schematic diagram of CDI cell.

2.4.2 Charge efficiency

Charge efficiency (Λ) was calculated by Eq. (3):

$$\Lambda = \frac{\Gamma \cdot F}{\Sigma}$$

Where Γ is the electrosorption capacity (mol g^{-1}), F is the Faraday constant (96485 C mol^{-1}) and Σ (charge, C g^{-1}) is obtained by integrating the corresponding current.

2.4.3 Kim-Yoon plot

To evaluate the electrosorption capacity and electrosorption rate of CDI electrodes [21], Kim-Yoon plot is effective method. At that t (min), the electrosorption capacity (Γ_t, mg g^{-1}) was calculated by Eq. (4):

$$\Gamma_t = \frac{(C_0 - C_t) \cdot V}{m}$$

In electrosorption process, the mean electrosorption rate (v_t, mg g^{-1} min^{-1}) at t (min) of the CDI electrode is calculated by Eq. (5):

$$v_t = \frac{\Gamma_t}{t}$$

2.4.4 Energy consumption

The energy consumption (E_{ads}, kJ mol^{-1}) per desalinated ions during the electrosorption process was calculated by Eq. (6):

$$E_{ads} = \frac{V \cdot \int I dt}{\int (C_t - C_0) \cdot \Phi \cdot dt}$$

Where V is the applied voltage (V), I is the current (A), t is the adsorption time (s), C_t is the NaCl concentration (M) at time (s), C_0 is the initial NaCl concentration (M) and Φ is the flow rate (L s^{-1}).

2.4.5 Relationship between conductivity and concentration

Fig. 2.3 shows the relationship between NaCl solution concentration (mg L^{-1}) and NaCl solution conductivity (μS cm^{-1}). Relationship equation follows linear plot and is presented as:

$$Y = 2.328X + 3$$

Where X and Y are NaCl solution concentration and NaCl solution conductivity, respectively. The correlation coefficient (R^2) of this equation is 0.9993.

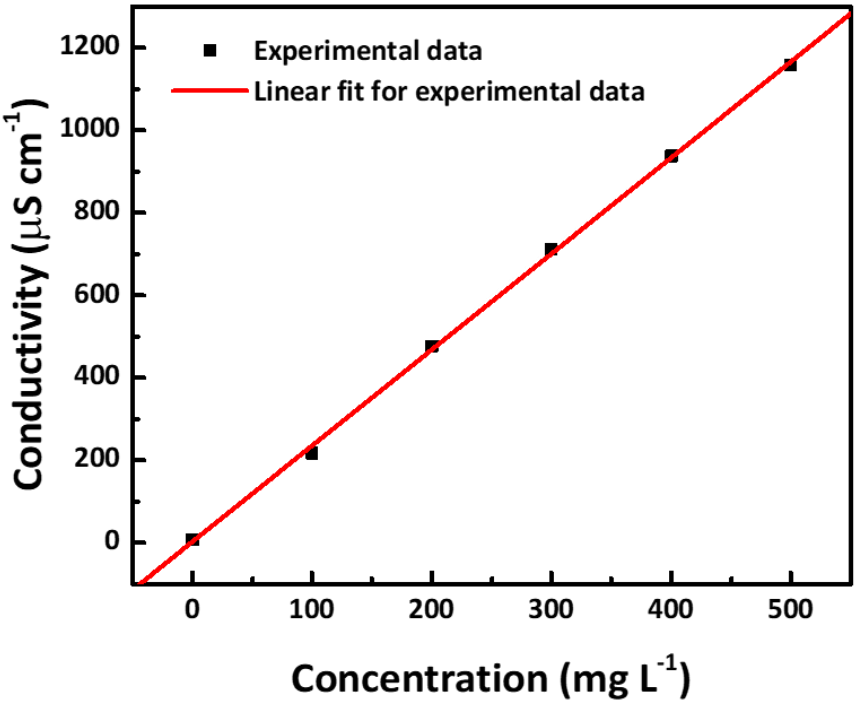

Figure 2.3. Relationship between the concentration (mg L^{-1}) and the conductivity (μS cm^{-1}) of NaCl solution.

Chapter 3. Results and discussion

3.1 Characterization

The activated carbon (AC) as reference material is chosen because AC is normally used in CDI application. To check the morphology of AC and mm-PGS, the scanning electron microscopy (SEM) and transmission electron microscopy (TEM) images were analyzed. The larger size porous property of mm-PGS compared to AC (Fig. 3.2) was shown in Fig. 3.1(a). The inset in Fig. 3.1(a) exhibits that many 20 nm spherical particles are agglomerated together to form whole structure. The TEM image in Fig. 3.1(b) exhibits that uniform mm-PGS particles are clustered and the inner part of mm-PGS is empty after etching silica templates. The inset in Fig. 3.1(b) reveals that many graphene are entangled and pores are enveloped by these graphene layer (3-7 layers), indicating that this property is advantageous for better electrical conductivity. The morphology of AC in Fig. 3.2 shows only existence of large particles compared to mm-PGS and then whole structure is unfavorable to ion transport.

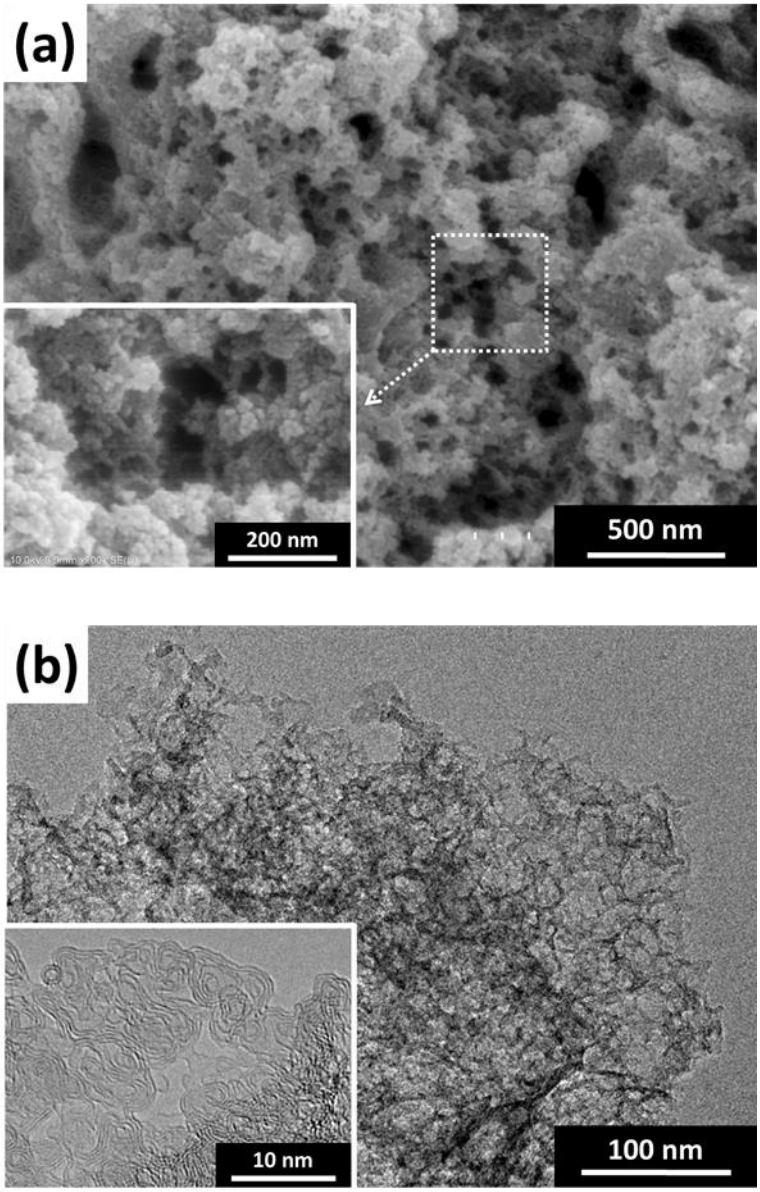

Figure 3.1. SEM (a) and TEM (b) images of mm-PGS. Insets in (a) and (b) show enlarged SEM and TEM image of mm-PGS, respectively.

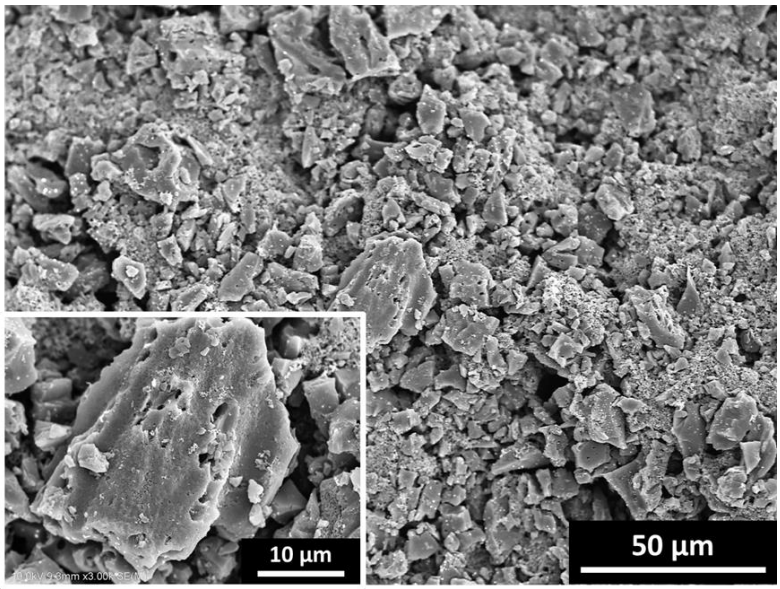

Figure 3.2. SEM images of AC. Inset shows enlarged SEM image of AC.

Internal structure information such as surface area and pore size is directly related to the electrosorption capacity. These information were acquired from nitrogen adsorption desorption isotherms. The isotherm of mm-PGS in Fig. 3.3(c) exhibits a typical type-IV property with hysteresis loop, indicating the existence of mesopore properties, while the isotherm of acitivated carbon in Fig. 3.3(a) shows type-I and type-IV combination property with small hysteresis loop because of the presence of some mesopores as shown in Fig. 3.2 SEM image. Through the Brunauer-Emmett-Teller method, specific surface area (SSA), pore volume and mean pore diameter were acquired and listed in Table 4.1. Obviously, mm-PGS shows a large surface area of 1492.8 $m^2 g^{-1}$ with a pore volume of 5.1198 $cm^3 g^{-1}$, indicating that this value is higher than results of AC (1322 $m^2 g^{-1}$ and 0.765 $cm^3 g^{-1}$). Furthermore, the pore size distribution of mm-PGS and AC in Fig. 3.3(b) and (d) shows that mm-PGS has micro, meso and macro properties, while AC is mainly composed of micropores.

According to SEM images in Fig. 3.1(a) and BET results in Table 4.1, the mm-PGS shows the microporous property which is derived from etching nickel clusters by HCl and HF, while mesoporous and macroporous properties of mm-PGS are derived by etching silica templates and nickel clusters. The existence of mesoporous structure is advantageous for ions accessibility from interface to inner part area during electrosorption process [10] and helps to induce the charge transfer to accelerate speed. [22] Thus, the mm-PGS is expected for CDI performance.

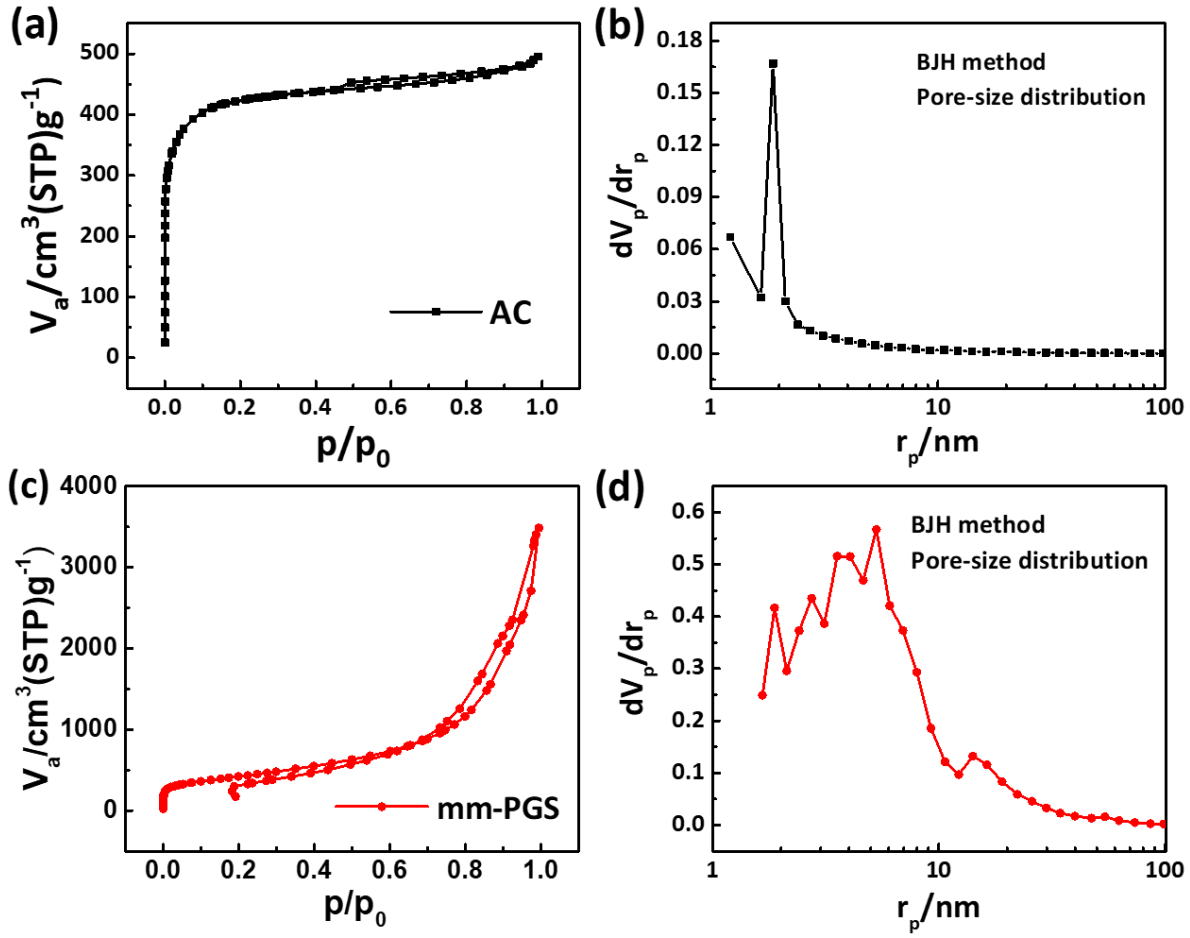

Figure 3.3. N_2 adsorption/desorption isotherm of (a) AC and (c) mm-PGS. Pore size distribution of (b) AC and (d) mm-PGS.

Table 3.1. Morphology information of AC and mm-PGS.

Sample	Specific surface area (m^2 g^{-1})	Pore volume (cm^3 g^{-1})	Mean pore diameter (nm)
AC	1322	0.765	2.3246
mm-PGS	1492.8	5.1198	13.719

Fig. 3.3(a) and (b) exhibit Raman spectrum of AC and mm-PGS, respectively. Both Raman spectrum show two peaks at 1344 and 1590 cm-1, indicating that the D band and the G band, respectively. The D band is associated with the existence of defects in carbon structure, while the G band is related with graphitic property of carbon. [10] The relative intensity ratio of D band to G band (I_D/I_G) shows the relative quantity of defects in the graphitic carbon, and corresponding I_D/I_G values for AC and mm-PGS are recorded in Fig. 3.3(a) and (b). The mm-PGS shows low I_D/I_G value (0.97) compared to AC (1.17), indicating that the mm-PGS has more graphitic structure which is favorable for the electrical conductivity. Additionally, powder conductivity experiments for samples were conducted to compare I_D/I_G results. According to the slope of I-V curve in Fig. 3.3(c), electrical conductivity results can be calculated. Fig 3.3(d) shows that the mm-PGS (11.36 S m^{-1}) has better electrical conductivity compared to AC (8.11 S m^{-1}), indicating that these results are consistent with tendency for I_D/I_G.

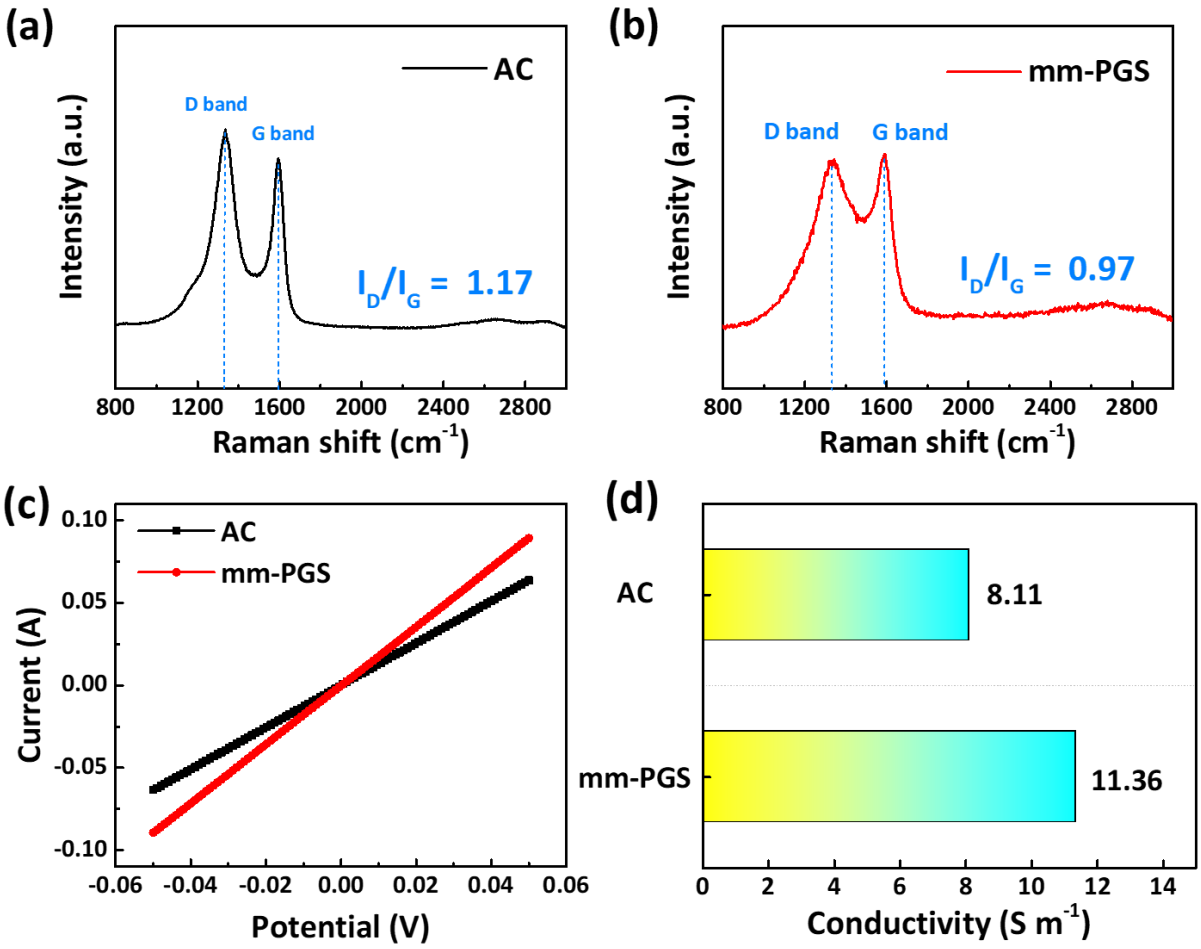

Figure 3.4. Raman spectra of (a) AC and (b) mm-PGS. Powder conductivity: (c) I-V data; (d) Electrical conductivity of AC and mm-PGS.

To acquire information of chemical structure for mm-PGS, the X-ray photoelectron spectroscopy (XPS) measurement was conducted. Fig. 3.4(a) shows XPS spectrum of mm-PGS from 0 to 600 eV binding energy, indicating that no impurities are observed and mm-PGS is composed by only carbon and oxygen atoms. The carbon and oxygen contents (At. %) in mm-PGS are listed in Table 4.2. Oxygen contents in carbon materials are advantageous for the hydrophobic property, indicating favorable electrolyte penetration from interface to inner part of carbon materials and efficient utilization of pores. From the C1s spectrum of mm-PGS in Fig. 3.4(b), XPS peaks are observed at 284.5, 285.0, 286.3, 287.7, 289.0 and 291 eV corresponding to sp^2 carbon, sp^3 carbon and oxygen-related functional group C-O, C=O, O-C=O, and pi-pi* interaction, respectively. [23, 24]

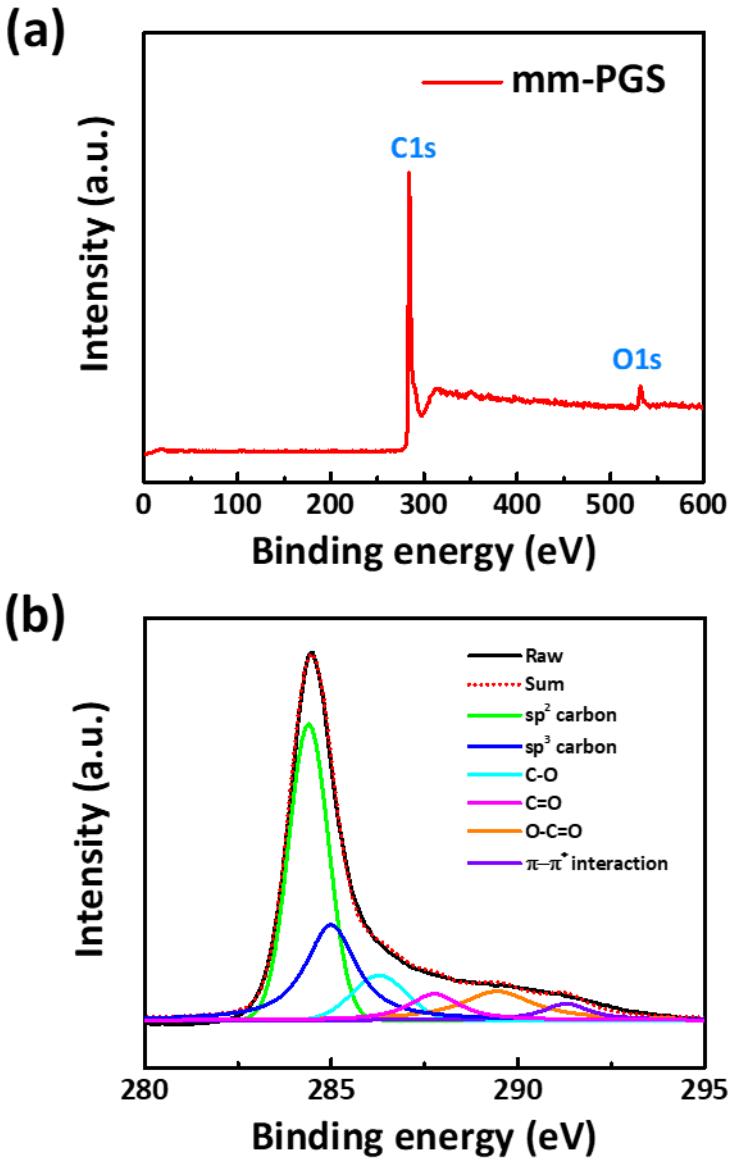

Figure 3.5. (a) XPS spectrum and (b) XPS C1s spectra of mm-PGS.

Table 3.2. The carbon and oxygen contents (At. %) in mm-PGS.

Sample	C (At. %)	O (At. %)
mm-PGS	95.14	4.86

3.2 Electrochemical results

Before electrosorption measurement, electrochemical test should be conducted by cyclic voltammetry (CV) and impedance electrical spectroscopy (EIS) with a 3-electrode system in 1 M NaCl solution. The thickness for all electrochemical electrodes was set to be 0.270~0.300 mm. For AC and mm-PGS electrode, Fig. 3.6(a) shows that CV curves are measured at 10 mV s^{-1} with electrical potential from -0.5 to 0.5 V. Both CV curves exhibit no faradaic peak and rectangular shape, indicating that both CV curves are operated by Electrical double layer (EDL) system at the interface between electrolyte and surface of active material. [25] mm-PGS and AC electrodes shows high current density because both electrodes have favorable condition (high surface area, >1300 m^2 g^{-1}) to form the EDL, while the mm-PGS electrode exhibits a larger CV area than the AC electrode. Though both samples have high surface area (1492.8 m^2 g^{-1} vs. 1322 m^2 g^{-1}, see Table 4.1.), meso/micro porous structure in mm-PGS affects ion mobility and leads large size CV curve compared to AC electrode. [10]

The specific capacitance was calculated by Eq. (1) (in 2.2.2. Cyclic voltammetry) and Fig 4.6(b) shows correlation graph between the specific capacitance and the scan rate for both samples. The mm-PGS electrode shows a larger capacitance (141 F g^{-1}) than the AC electrode (122 F g^{-1}) at a scan rate of 10 mV s^{-1}, suggesting that mm-PGS electrode has large capability for sodium and chlorine ions. The capacitance for carbon-based electrode is closely related to the pore volume and the surface area. For both electrodes under similar surface area, large pore volume is important factor to absorb ions, decreasing loss of electrical resistance and accelerating electron transfer. [22] The mm-PGS has larger pore volume of 5.1198 cm^3 g^{-1} compared to AC (0.765 cm^3 g^{-1}), while maintained graphene layers in mm-PGS are favorable for high electrical conductivity. Thus, mm-PGS shows large CV area and advantageous for absorbing large amount of salts.

The EIS measurement provides more information for electrochemical results. Nyquist profiles are shown in Fig. 3.7 with semicircle in high frequency region and straight line in low frequency region. [10] The charge transfer resistance (R_{ct}) at the interface between electrolyte and surface of active material is related to a semicircle in high frequency. The R_{ct} of mm-PGS electrode exhibits low value (0.3398 Ω) compared to activatd carbon electrode (0.7698 Ω), indicating that mm-PGS electrode has small charge-transfer resistance at interface. A slope of straight line in low frequency region corresponds to ions diffusion and represents and ideal capacitor. [10] A slope of mm-PGS electrode clearly is high value compared to AC electrode, indicating that mm-PGS has fast ions diffusion characteristic. Furthermore, the contact resistance (R_s) at interface between active material and current collector was

investigated under same experiment condition. The Rs of mm-PGS shows high value (2.585 Ω) compared to AC (2.090 Ω) because large pores in mm-PGS cause decrease in contact area between active material and current collector. Thus, R_s value for mm-PGS has high value. [26]

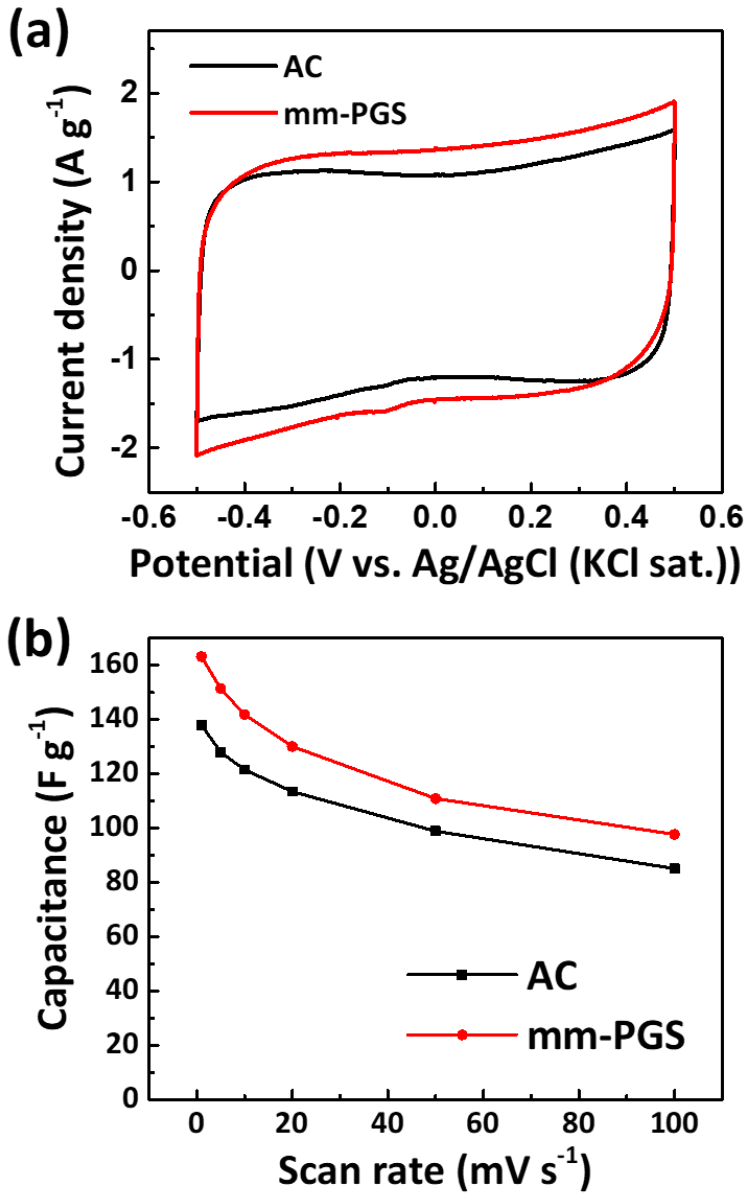

Figure 3.6. (a) CV curves at scan rate of 10 mV s^{-1}. (b) Specific capacitances of AC and mm-PGS electrode in 1 M NaCl solution at various scan rates.

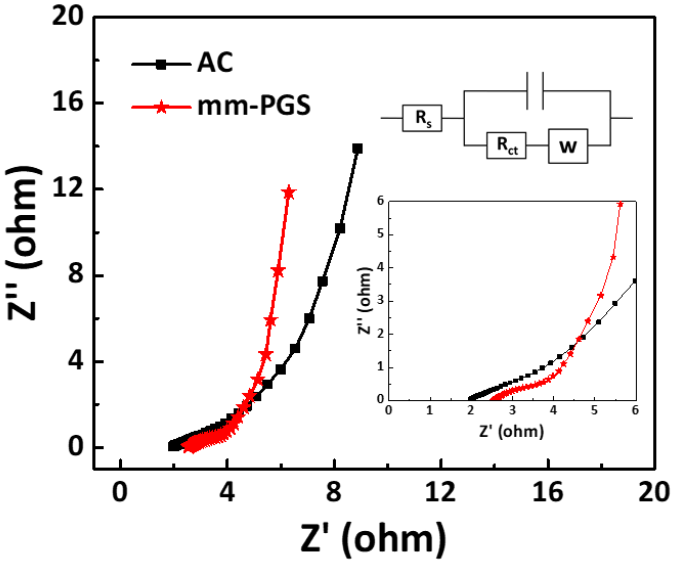

Figure 3.7. Nyquist profiles of AC and mm-PGS electrode in 1 M NaCl solution. Inset exhibits the corresponding equivalent electric circuit model and the expanded plots at high-frequency region.

3.3 Electrosorption results

The fabricated mm-PGS and AC were utilized as an active material for CDI electrodes which are measured under a 100 ppm NaCl solution at applied potential of 1.2 V. The NaCl solution was flowed through the nylon spacer that is positioned between two paralleled CDI electrodes and flow rate was 30 mL min^{-1}. When the potential applied to two electrodes, sodium and chlorine ions moves into EDL on cathode and anode, respectively. Thus, concentration of NaCl solution decreased until electrode saturation state (equilibrium state). To desorb ions from CDI electrode, 0 V applied to two opposite electrodes. Fig. 3.8 shows a conductivity-time graph of mm-PGS electrode for 1 cycle and illustrates above adsorption-desorption process.

Fig. 3.9(a) exhibits the electrosorption capacity (EC)-time graph for AC and mm-PGS electrodes. EC values of AC and mm-PGS under 100 ppm NaCl solution were calculated using the Eq. (2) (in 2.3.1 Experiment condition and electrosorption capacity) and listed in Table. 4.3. mm-PGS electrode rapidly reached the equilibrium state until 10 minutes and shows high EC result (9.37 mg g^{-1}), while AC electrode exhibits long time (~23 minutes) to reach saturation state and shows lower EC result (8.07 mg g^{-1}) than mm-PGS electrode. Thus, mm-PGS electrode shows fast electrosorption rate and large electrosorption capacity compared to AC electrode.

To evaluate the desalination performance, Kim-Yoon plot is used as effective criterion for CDI electrodes. Fig. 3.9(b) indicates Kim-Yoon plots for AC and mm-PGS electrodes. mm-PGS electrode shows fast mean electrosorption rate (MER, 2.79 mg g^{-1} min^{-1}) and rapidly reaches the equilibrium state (9.37 mg g^{-1}), indicating that large pores and better electrical conductivity of mm-PGS are advantageous for fast desalination and high CDI performance. [27]

The EC for mm-PGS electrode was measured under various initial concentration (100, 250 and 500 ppm) of NaCl solution at 1.2 V. Fig. 3.10 shows that the EC increases from low concentration to high concentration of NaCl solution, thus mm-PGS electrode shows highest EC value (11.74 mg g^{-1}) at 500 ppm of NaCl solution. The improvement of EC as the increase in concentration of NaCl can be described as the decrease in EDL overlapping effect and enhancement of ion transfer inside pores. [28]

The charge efficiency (Λ) is key information for electrical double layer and is defined as the ratio of EC value multiplied by faradaic constant and electrode charge during CDI process. [29] As in Table. 4.3, the Λ of AC and mm-PGS were calculated using the Eq. (3) (in 2.3.2. Charge efficiency) is 0.76 and 0.29, respectively. These results indicate that mm-PGS efficiently forms electrical double layer

interface on surface of porous carbon in NaCl solution and is promising carbon material for CDI electrode.

Fig. 3.10 shows the electrosorption-desorption cycles of mm-PGS electrode under repeated applying potential (Charge (1.2 V)-Discharge (0 V)) in 100 ppm NaCl solution. The mm-PGS electrode clearly regenerated and re-adsorbed ions for over 5 cycles.

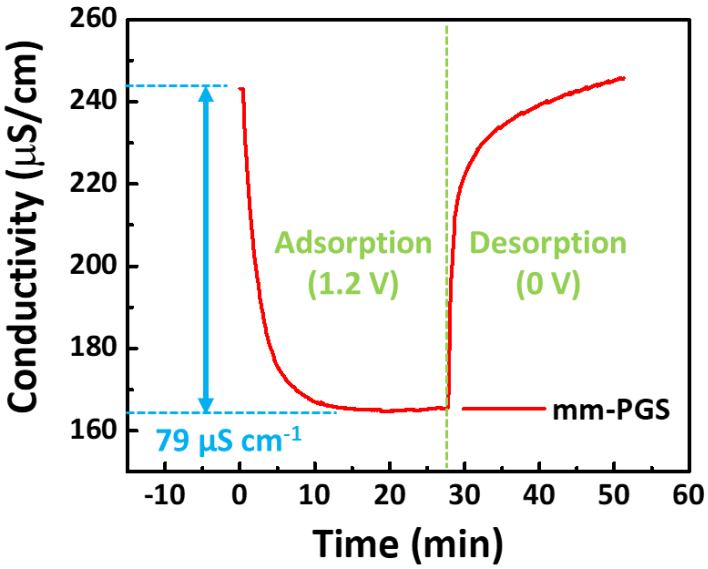

Figure 3.8. Electrosorption-desorption behavior of mm-PGS electrode with an initial concentration of ~100 ppm NaCl solution.

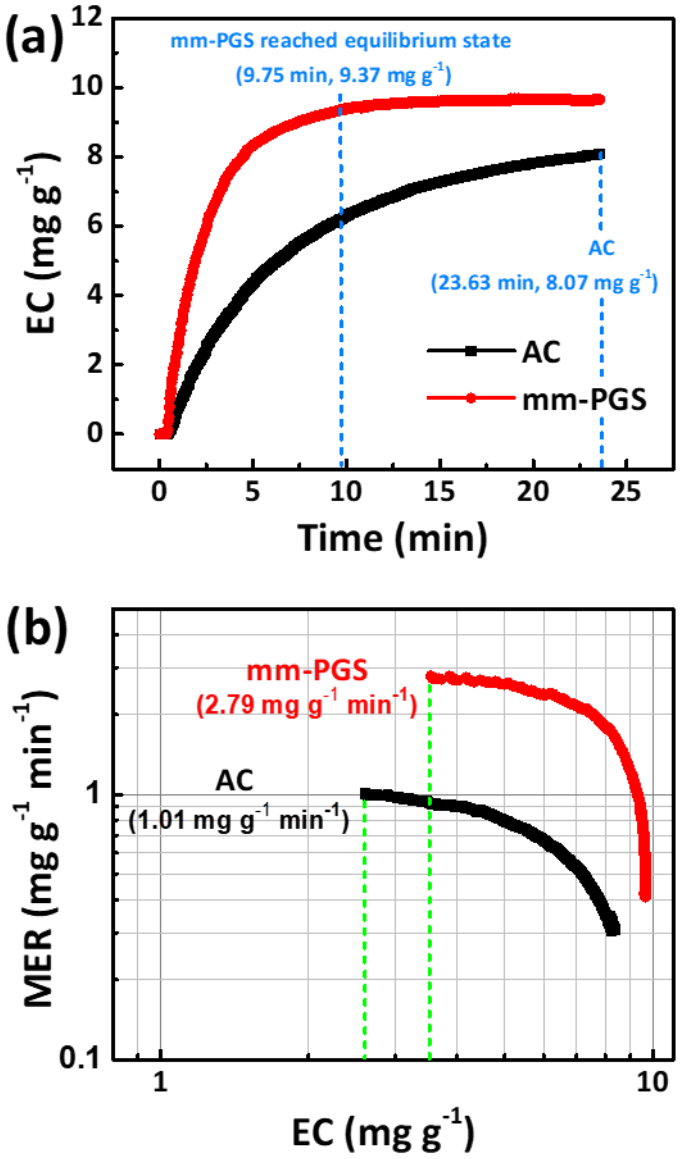

Figure 3.9. (a) Electrosorption capacity-time curves and (b) Kim-Yoon plots of AC and mm-PGS electrode in a 100 ppm NaCl solution.

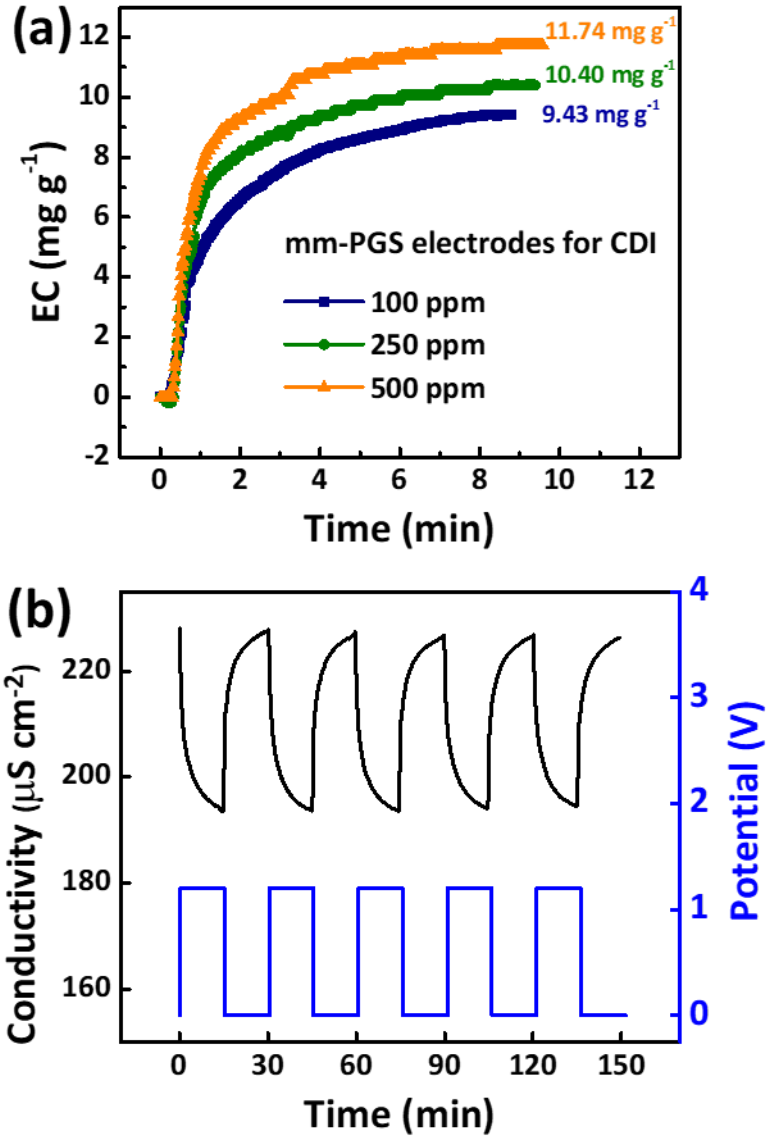

Figure 3.10. (a) Electrosorption capacity of mm-PGS electrode with different initial concentrations (100, 250 and 500 ppm) at an applied voltage of 1.2 V and (b) Recycle electrosorption performance of mm-PGS electrode in a 100 ppm NaCl solution.

Table 3.3. Electrosorption capacities, maximum MER and charge efficiencies of AC and mm-PGS electrode in 100 ppm NaCl solution.

	EC ($mg\ g^{-1}$)	Maximum MER ($mg\ g^{-1}\ min^{-1}$)	Charge efficiency (Λ)
AC	8.07	1.01	0.29
mm-PGS	9.37	2.79	0.76

3.4 Kinetic study of electrosorption

Our study chose the pseudo-first-order and the pseudo-second-order kinetic models to investigate the adsorption rate constant for AC and mm-PGS electrodes in more detail. Both kinetic models are utilized to fit adsorption kinetic for active materials and equations are described as:

$$\log(q_e - q_t) = \log q_e - \frac{k_1 t}{2.303} \qquad \text{Pseudo-first-order} \qquad (1)$$

$$\frac{t}{q_t} = \frac{1}{k_2 q_e^2} + \frac{t}{q_e} \qquad \text{Pseudo-second-order} \qquad (2)$$

Where k_1 (mg g^{-1} min^{-1}) and k_2 (mg g^{-1} min^{-1}) are the adsorption rate constant for the pseudo-first-order and the pseudo-second-order, respectively. q_e (mg g^{-1}) and q_t (mg g^{-1}) are the quantity of adsorbed NaCl at equilibrium state and time t (min), respectively. [30] Fig. 3.11(a) and (b) show linear fitting graphs for experiment results and kinetic equations. As listed in Table 3.4, quantity of adsorbed NaCl at q_e, adsorption rate constants and correlation coefficient (R_2) are calculated by slope and y-intercept which are acquired from predicted equation by kinetic model and experiment results. [31] Approximation of R^2 to 1 normally supports the assumption of kinetic model for the adsorption step. [32] According to Fig. 3.11 (a), (b) and R^2 values, the pseudo-second-order as kinetic model is more suitable for description of electrosorption activity for AC and mm-PGS electrode than the pseudo-first-order. From pseudo-second-order model, the adsorption rate constant of AC and mm-PGS is 0.01350 and 0.07146, respectively. Thus, the mm-PGS electrode shows high value of the adsorption rate constant compared to the AC electrode

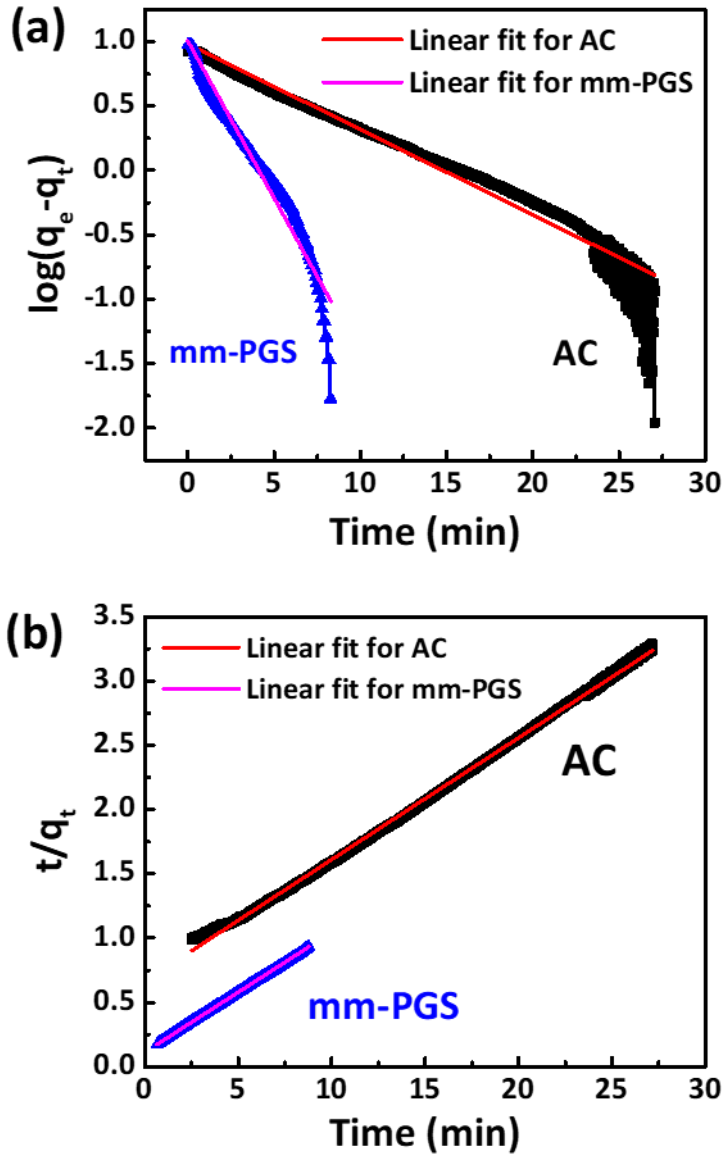

Figure 3.11. Linear fit of electrosorption behaviors of NaCl by AC and mm-PGS electrodes using (a) the pseudo-first-order kinetic model and (b) the pseudo-second-order kinetic model.

\

Table 3.4. The electrosorption parameters of the pseudo-first-order and the pseudo-second-order kinetic models.

Samples	Pseudo-first-order			Pseudo-second-order		
	q_e	k_1	R^2	q_e	k_2	R^2
AC	9.58	0.15269	0.9490	10.56	0.01350	0.9986
mm-PGS	10.12	0.56170	0.9453	10.86	0.07146	0.9999

3.5 Ion transport and mean electrosorption rate of mm-PGS

To explain fast electrosorption rate of mm-PGS electrode compared to AC electrode, schematic illustration of ion transport is described in Fig. 3.12. The AC has only large carbon particles through SEM images in Fig 3.1(a) and little meso and no macro channel to connect the inner part from interface, indicating that the ion transport is not favorable in AC. On the other hand, mm-PGS has mesopore and macropore channels which can effectively diffuse ions. [10] Also, large holes in mm-PGS can help electrolyte penetration from interface to inner part, suggesting that mm-PGS has good structure for fast ion adsorption. [27]

Fig. 3.13 exhibits the MER of various CDI materials to compare our mm-PGS. Obviously, mm-PGS shows fast electrosorption rate (0.96 mg g^{-1} min^{-1}) among reported CDI materials and this MER value is quite similar to mesoporous carbon (1.08 mg g^{-1} min^{-1}), indicating that mm-PGS is promising material for fast electrosorption.

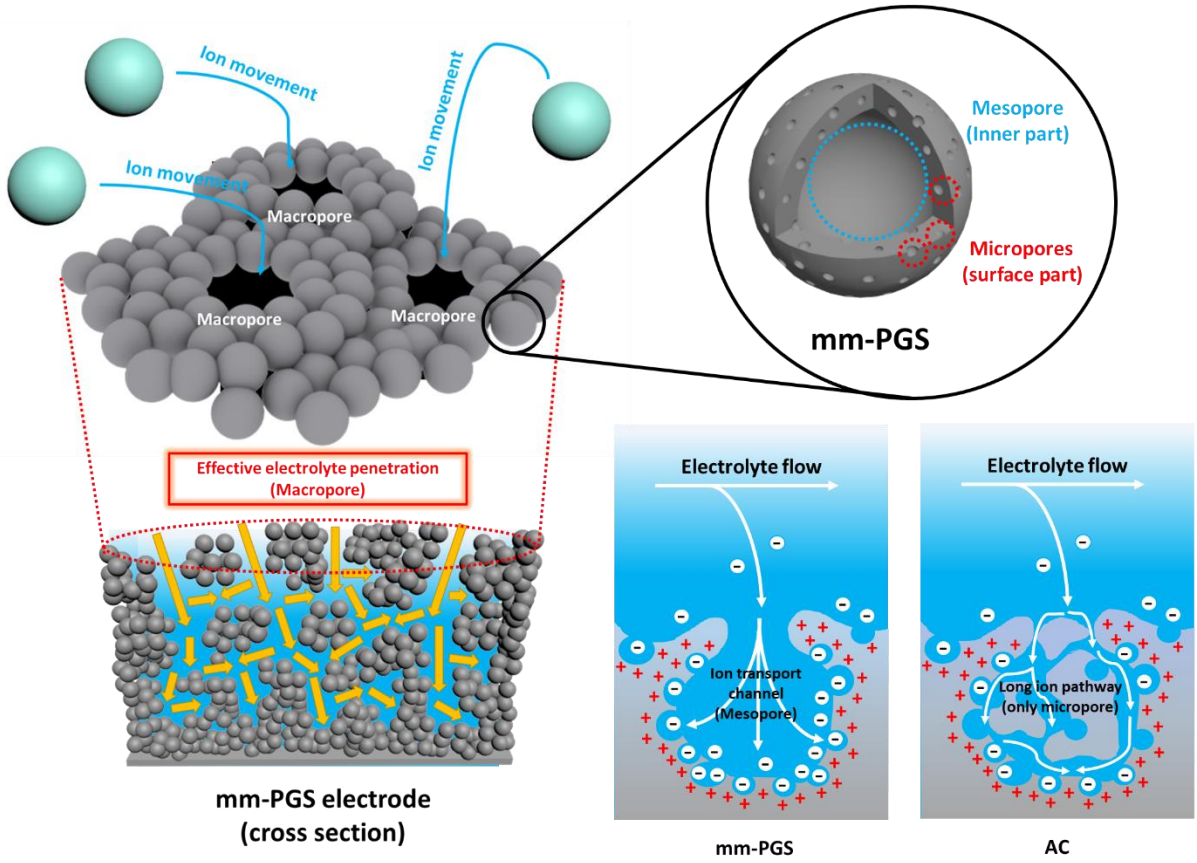

Figure 3.12. The schematic illustration of ion transport in the mm-PGS electrode.

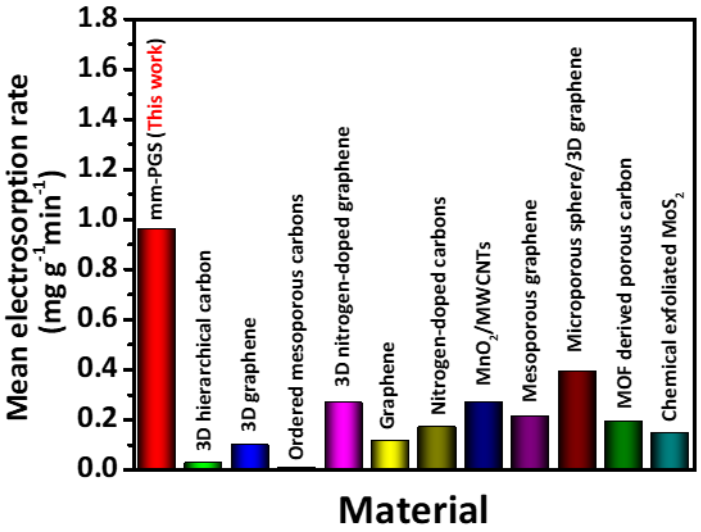

Figure 3.13. Comparison of mean electrosorption rate (mg g^{-1} min^{-1}) for various CDI materials (data taken from Table. 3.5.)

Table. 3.5 Mean electrosorption rate of various CDI materials.

Materials	Time (min)	Γ (mg g^{-1})	Mean electrosorption rate (mg g^{-1} min^{-1})	References
mm-PGS	9.75	9.37	0.96	This work
3D hierarchical carbon	80	2.16	0.027	J. Mater. Chem. 2012, 22 (45), 23835−23844.
3D graphene	55	5.39	0.098	J. Mater. Chem. A, 2013, 1 (38), 11778−11789.
Ordered mesoporous carbon	90	0.677	0.008	Water Res. 2008, 42 (8), 2340−2348.
3D nitrogen-doped graphene	30	8.04	0.268	Sci. Rep. 2015, 5, 11225.
Graphene	12	1.35	0.113	Environ. Sci. Technol. 2010, 44 (22), 8692−8697.
Nitrogen-doped carbons	50	8.52	0.17	Sci. Rep. 2016, 6, 28847.
MnO_2/MWCNT	25	6.65	0.27	RSC Adv. 2016, 6 (8), 6730−6736.
Mesoporous graphene	30	6.38	0.213	Electrochimica Acta 188 (2016) 406–413
Microporous sphere/3D graphene	25	9.86	0.394	Electrochimica Acta 193 (2016) 88–95
MOF derived porous carbon	40	7.71	0.193	Chem. Commun., 2015, 51, 12020-12023
Chemical exfoliated MoS_2	60	8.81	0.147	Nano Energy 31 (2017) 590–595

3.6 Energy consumption

Fig. 3.14 shows the energy consumption per desalination ion of AC electrode and mm-PGS electrode under 100 ppm NaCl solution at applied potential 1.2 V. According to Eq. (6) (in 2.3.4. Energy consumption), mm-PGS electrode needed 23.61 kilo joule for absorbing one mole of NaCl and this value is lower than AC electrode (176.69 kJ mol^{-1}). mm-PGS electrode rapidly reached the equilibrium state by meso/macro transport channel, indicating that this property can be decrease consuming electrical energy for short time. Thus, mm-PGS electrode consumed low electrical energy compared to AC electrode and mm-PGS is promising material for CDI industry.

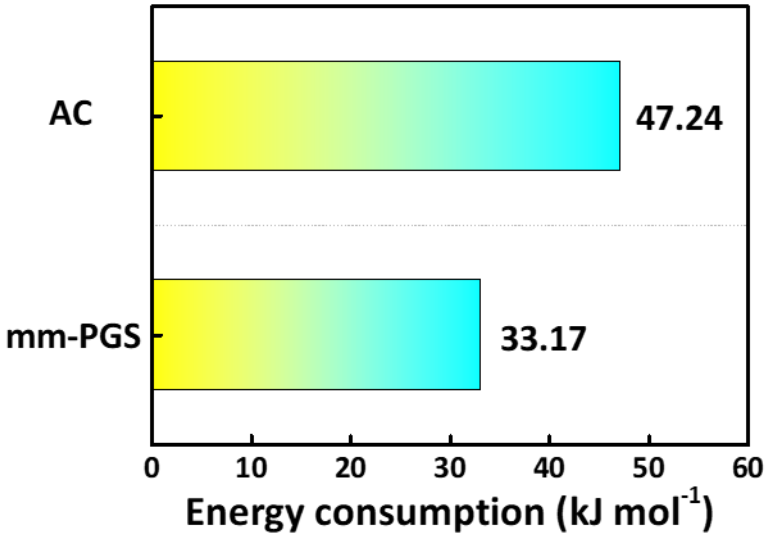

Figure 3.14. Energy consumption of AC and mm-PGS electrodes with an initial concentration of ~100 ppm NaCl solution.

3.7 Etc.

De-functionalization by heat and hydrogen treatment is effective method to enhance the CDI performance. [33] Fig. 3.15 exhibits thermo-gravimetric analysis (TGA) curves for mm-PGS before 2 nd pyrolysis (B-mm-PGS, black line) and mm-PGS after 2 nd pyrolysis (A-mm-PGS, red line) from room temperature to 900 degree with a ramping rate (10 ^{o}C min^{-1}) and N_2 atmosphere. Weight of B-mm-PGS was continuously decrease when TGA temperature increases, indicating that functional groups are lost by heat treatment and many functional groups on surface of B-mm-PGS are formed by HF and HCl etching process. On the other hand, TGA curve of A-mm-PGS shows no remarkable weight loss until 900 degree, indicating de-functionalization of mm-PGS.

Our synthesis strategy of mm-PGS can yield gram scale of carbon material. Fig. 3.16 shows photographic image of 40 ml glass vial which contains 1.0 g of mm-PGS sample per one fabrication time. In CDI technology which requires a large amount of carbon material, our synthesis method of mm-PGS is advantageous for the CDI field.

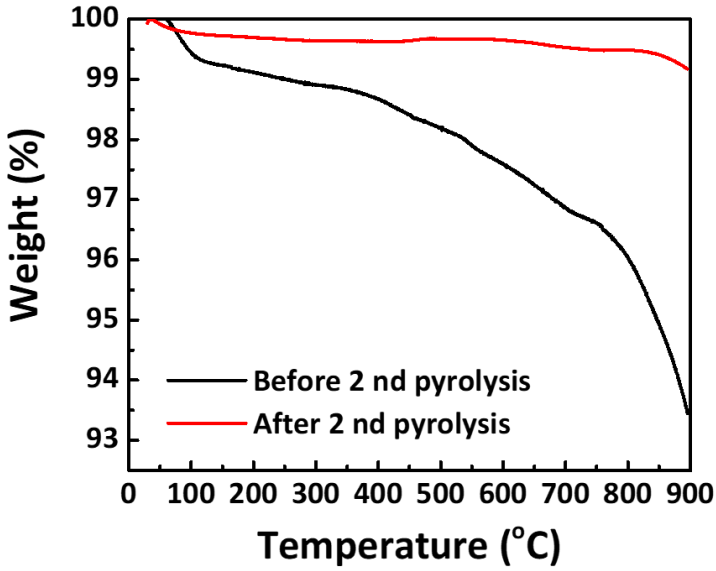

Figure 3.15. TGA curves of mm-PGS. Before 2 nd pyrolysis (black line) and after 2 nd pyrolysis (red line).

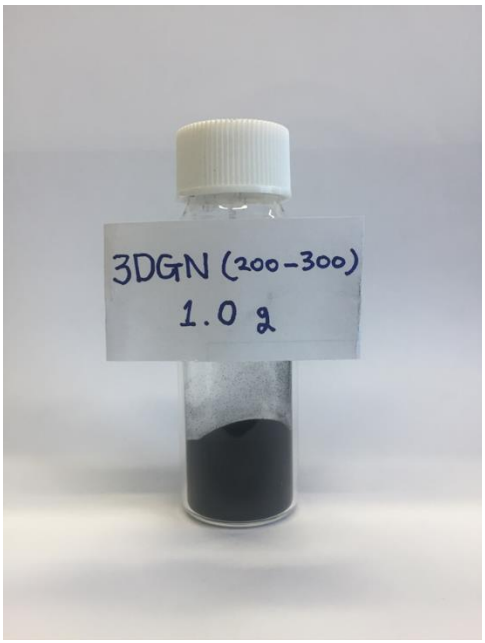

Figure 3.16. Photographic image of 40 mL glass vial filled by mm-PGS sample (1.0 g).

Chapter 4. Conclusion

In summary, the mm-PGS was synthesized through silica template strategy with $NiCl_2$ and PVA as catalyst and carbon precursor, respectively. Also, this fabrication strategy solves the quantity problem of active material in CDI field (Gram scale production of mm-PGS). The mm-PGS has high specific surface area and micro/meso/macro porous morphology, indicating that these properties are favorable for ion transport and ion accumulation. The experimental results exhibit that (i) the mm-PGS electrode achieves a remarkable desalination rate (Maximum MER: 2.79 mg g^{-1} min^{-1}) and performance with a high electrosorption capacity of 9.37 mg g^{-1} under 100 ppm NaCl solution; (ii) According to kinetic model (Pseudo-second-order), rapid electrosorption rate of mm-PGS was reconfirm; (iii) meso/macro porous structure of mm-PGS is favorable for electrolyte penetration and ion transport from interface to inner part of carbon materials; (iv) the mm-PGS consumed low energy consumption (23.61 kJ mol^{-1}) compared with activated carbon (176.69 kJ mol^{-1}). Therefore, the mm-PGS is promising porous carbon material for low energy consumption, fast desalination, gram scale production and high desalination performance

REFERENCES

1. Thu, K., *Adsorption desalination: theory & experiments*. 2010.
2. AlMarzooqi, F.A., et al., *Application of capacitive deionisation in water desalination: a review.* Desalination, 2014. **342**: p. 3-15.
3. *Water Desalination Market Size and Forecast, By Technology (Reverse Osmosis, Multi-Stage Filtration, Multi-Effect Distillation), By Source (Seawater, Brackish Water, Wastewater), And Trend Analysis, 2014 - 2025*. 2017: Hexa Research.
4. Porada, S., et al., *Review on the science and technology of water desalination by capacitive deionization.* Progress in Materials Science, 2013. **58**(8): p. 1388-1442.
5. Helmholtz, H.v., *Annalen der Physik.* Leipzig, 1853. **89**: p. 21.
6. Gouy, M., *Sur la constitution de la charge électrique à la surface d'un électrolyte.* J. Phys. Theor. Appl., 1910. **9**(1): p. 457-468.
7. Chapman, D.L., *LI. A contribution to the theory of electrocapillarity.* The London, Edinburgh, and Dublin philosophical magazine and journal of science, 1913. **25**(148): p. 475-481.
8. Stern, O., *Zur theorie der elektrolytischen doppelschicht.* Berichte der Bunsengesellschaft für physikalische Chemie, 1924. **30**(21- 22): p. 508-516.
9. Zhang, L.L. and X. Zhao, *Carbon-based materials as supercapacitor electrodes.* Chemical Society Reviews, 2009. **38**(9): p. 2520-2531.
10. Xu, X., et al., *Design and fabrication of mesoporous graphene via carbothermal reaction for highly efficient capacitive deionization.* Electrochimica Acta, 2016. **188**: p. 406-413.
11. Li, H., et al., *Novel graphene-like electrodes for capacitive deionization.* Environmental science & technology, 2010. **44**(22): p. 8692-8697.
12. Zhang, D., et al., *Preparation and desalination performance of multiwall carbon nanotubes.* Materials Chemistry and Physics, 2006. **97**(2-3): p. 415-419.
13. Wang, G., et al., *Activated carbon nanofiber webs made by electrospinning for capacitive deionization.* Electrochimica Acta, 2012. **69**: p. 65-70.
14. Oh, H.-J., et al., *Nanoporous activated carbon cloth for capacitive deionization of aqueous solution.* Thin Solid Films, 2006. **515**(1): p. 220-225.
15. Li, J., et al., *Studies on preparation and performances of carbon aerogel electrodes for the application of supercapacitor.* Journal of Power Sources, 2006. **158**(1): p. 784-788.
16. Peng, Z., et al., *Comparative electroadsorption study of mesoporous carbon electrodes with various pore structures.* The Journal of Physical Chemistry C, 2011. **115**(34): p. 17068-17076.

17. Chabot, V., et al., *A review of graphene and graphene oxide sponge: material synthesis and applications to energy and the environment.* Energy & Environmental Science, 2014. **7**(5): p. 1564-1596.
18. Singh, V., et al., *Graphene based materials: past, present and future.* Progress in materials science, 2011. **56**(8): p. 1178-1271.
19. Li, J., et al., *Hierarchical hole-enhanced 3D graphene assembly for highly efficient capacitive deionization.* Carbon, 2018. **129**: p. 95-103.
20. Huang, Z.-H., et al., *Carbon electrodes for capacitive deionization.* Journal of Materials Chemistry A, 2017. **5**(2): p. 470-496.
21. Kim, T. and J. Yoon, *CDI ragone plot as a functional tool to evaluate desalination performance in capacitive deionization.* RSC Advances, 2015. **5**(2): p. 1456-1461.
22. Wen, Z., et al., *Crumpled nitrogen‐doped graphene nanosheets with ultrahigh pore volume for high‐performance supercapacitor.* Advanced Materials, 2012. **24**(41): p. 5610-5616.
23. Okpalugo, T., et al., *High resolution XPS characterization of chemical functionalised MWCNTs and SWCNTs.* Carbon, 2005. **43**(1): p. 153-161.
24. Girard-Lauriault, P.-L., et al., *Surface functionalization of graphite and carbon nanotubes by vacuum-ultraviolet photochemical reactions.* Applied Surface Science, 2012. **258**(22): p. 8448-8454.
25. Xu, X., et al., *Hierarchical hybrids with microporous carbon spheres decorated three-dimensional graphene frameworks for capacitive applications in supercapacitor and deionization.* Electrochimica Acta, 2016. **193**: p. 88-95.
26. Qu, Y., et al., *Characterization of resistances of a capacitive deionization system.* Environmental science & technology, 2015. **49**(16): p. 9699-9706.
27. Tang, K., et al., *Macropore-and Micropore-Dominated Carbon Derived from Poly (vinyl alcohol) and Polyvinylpyrrolidone for Supercapacitor and Capacitive Deionization.* ACS Sustainable Chemistry & Engineering, 2017. **5**(12): p. 11324-11333.
28. Li, Y., et al., *Design of nitrogen-doped cluster-like porous carbons with hierarchical hollow nanoarchitecture and their enhanced performance in capacitive deionization.* Desalination, 2018. **430**: p. 45-55.
29. Zhao, R., et al., *Charge efficiency: a functional tool to probe the double-layer structure inside of porous electrodes and application in the modeling of capacitive deionization.* The Journal of Physical Chemistry Letters, 2009. **1**(1): p. 205-210.
30. Wang, H., et al., *Design of graphene-coated hollow mesoporous carbon spheres as high*

performance electrodes for capacitive deionization. Journal of Materials Chemistry A, 2014. **2**(13): p. 4739-4750.

31. Liu, Y., et al., *Electrospun carbon nanofibers reinforced 3D porous carbon polyhedra network derived from metal-organic frameworks for capacitive deionization.* Scientific reports, 2016. **6**: p. 32784.
32. Li, H., et al., *A comparative study on electrosorptive behavior of carbon nanotubes and graphene for capacitive deionization.* Journal of Electroanalytical Chemistry, 2011. **653**(1-2): p. 40-44.
33. Krüner, B., et al., *Hydrogen-treated, sub-micrometer carbon beads for fast capacitive deionization with high performance stability.* Carbon, 2017. **117**: p. 46-54.

ACKNOWLEDGEMENT

저는 2015년 7월에 처음으로 UNIST에 왔습니다. 그리고 1년 동안 연구원 생활을 한 후에 석사 과정으로 들어와서 2016년 9월부터 2018년 지금까지 석사과정을 보냈습니다. 3년동안 느낀 것은 공부를 하면 할수록 모르는 게 너무 많다는 것이었습니다. 아직도 전 부족하지만 부족한 저를 도와주는 여러 사람들이 있었기에 석사과정을 마치고 올해 가을부터 다시 박사과정이라는 긴 여정을 도전하려고 합니다.

저를 처음 거두어주시고 지도해주신 우리 SSEL 연구실 장지현 교수님 감사합니다. 바쁘신 와중에도 불구하고 학위 디펜스에 참여해 주신 송현곤 교수님, 박종남 교수님 감사합니다. 옆에서 남 모르게 많이 도와주신 우리 연구실 선이 누나 감사합니다. 우리 연구실 랩실 멤버 종철이형, 성욱이형, 익희형, 기용이형, 종하형, 진욱, 명준, 광현, 경남, 성지, 철원, 재은, 선영, 수희, 주형, 세영 모두에게 감사합니다. 그리고 함께 대학원 생활 하는 옆 연구실 병준이형, 동규형도 감사합니다.

저의 석사 과정 중에 생긴 여러 고민을 들어준 우리 화학과 계모임 주기율표 멤버들, 09학번 동기들, 꿀화학과 집부 멤버들, 같이 영화토론 하는 친구들 감사합니다. 특히 제가 처음 UNIST 갈 때 도움을 많이 주신 원태진 교수님, 이제 곧 미국으로 유학가는 잔디, 강원도에서 열심히 씩씩하게 일하는 진화, 금요일 퇴근 때마다 전화해주는 도훈이, 창원 갈 때 마다 시간 내주는 대현이, 태희 저를 응원해줘서 감사했습니다

마지막으로 저에게 가장 중요한 존재인 아버지, 어머니, 동생 우리 가족 너무너무 감사합니다.

앞으로도 긴 박사과정 좋은 사람들과 힘내서 마쳐보도록 하겠습니다. 모두 사랑합니다 그리고 감사합니다.